Millimeter-Wave Slot-Based Cavity Antennas with Flexibly-Chosen Linear Polarization

Shu-Lin Chen, Geng-Bo Wu, Hang Wong, *Senior Member, IEEE,* Bao-Jie Chen, Chi Hou Chan, *Fellow, IEEE,* and Y. Jay Guo, *Fellow, IEEE*

***Abstract*—Slot-based cavity antennas are hailed as promising candidates for millimeter-wave applications. Nevertheless, the linear-polarization (LP) angle of their broadside main beam is limited by the slots etched on the cavity's top surface. In this work, an innovative technique is developed to significantly improve the selection flexibility of their LP inclination angle. It is attained by an integration of a single-layer, closely-spaced C-shaped patch surface. A TE_{710}-mode slot-based cavity antenna is employed as the base configuration, which radiates a broadside beam with its LP along $\phi = 90^\circ$. To effectively predict and monitor the polarization conversion of the surface-integrated TE_{710}-mode cavity antenna, an analysis method using a unit cavity extracted from its original cavity antenna is presented. A subsequent surface-integrated system with the specified 45°-LP was then simulated, fabricated, and measured. The measured results validate that a 45°-LP state is achieved with an operating bandwidth from 33.3 to 36.5 GHz. Further investigation is conducted to flexibly choose the LP direction from $\phi = 15^\circ$ to 165°. Two more examples with the fabricated antenna prototypes successfully radiate the specified $\phi = 15^\circ$ and 75° LP beam, respectively. This near-field polarization conversion surface can be generalized to cavities with different resonant modes.**

***Index Terms*—Cavity antenna, millimeter-wave (mm-wave), near-field, polarization conversion.**

I. Introduction

5G and beyond wireless communications are supposed to deliver large bandwidths and high data rates ranging from hundreds of Mbps to several Gbps. Millimeter-wave (mm-wave) antennas, which operate at high frequencies from 30 to 300 GHz, have been considered as one key enabled technology [1]–[8]. On the other hand, several hardware challenges are posed to apply those mm-wave antennas in communications systems, such as being low-profile and easy-integration. Slot-based cavity antennas are promising candidates due to their low loss, low profile, and simple structure [9]–[11].

A variety of advanced designs have been reported to improve functionalities of the mm-wave slot-based cavity antennas, including wide operating bandwidth [12]–[15], high gain [16], [17], and multiple beams [18]. One may find that all of the above linear-polarization (LP) slot-based cavity antennas have their polarization directions being determined and limited by the slots etched on the cavity's top surface. Assuming the slot-based cavity antenna serves as a receiving antenna for an incoming LP wave in point-to-point communications, a critical feature of the receiving antenna is to match/align its LP with that of the incoming wave. Two main issues will arise if the polarization mismatch occurs. The first would be the gain loss (in dB), which is known to be $|20\log(\cos\phi_d)|$ with ϕ_d being the LP angle difference between the incoming and the receiving waves. For example, the gain loss will be around 3.0 dB when $\phi_d = 45^\circ$. The second is the cross-polarization (x-pol) deterioration, and the theoretical x-pol level (in dB) is $-|20\log(\cot\phi_d)|$ if both the receiving antenna and the incoming wave are ideally linearly-polarized. When $\phi_d = 45^\circ$, the x-pol level will be deteriorated seriously, i.e., the x-pol component is the same as the co-polarization (co-pol) one. It thus requires a flexible control on the LP direction of the slot-based cavity antennas to minimize potential polarization mismatch.

One straightforward method is to etch inclined slots on the cavity and vary the LP state by changing the slot inclination angle. However, the accumulated impedance of these in-series inclined slots limits the number of the radiating slots [19]. Special techniques, such as the alternating inductive and capacitive loading [20], substrate-integrated coaxial line [21] or the dielectric resonator antenna [22], must be employed for an impedance-matched, high-gain behavior when a large number of the slot elements are employed. These techniques in [20]–[22] usually discussed and realized 45°-inclined LP for the slot-based cavity antennas. One may also opt to utilize polarizers to control an antenna's far-field polarization [23]–[32]. A polarization rotator with multi-layered metal wire strips was developed in [31] to accomplish a 90°-polarization rotation, i.e., converting its x-pol. component into the co-pol one. It is found that most of those reported polarizers are 90°-polarization rotators.

Few papers were reported to discuss and investigate the realization of a flexibly-chosen LP. An arbitrary LP conversion was attained in [32] by employing a meander-line-based polarizer. It utilized eight equal-spaced metallic layers, and a number of parallel meander-line strips were uniformly printed on each layer. This eight-layered meander-line structure is complex. Furthermore, the meander-line polarizer is always located at far-field from the source antenna, while a low-profile flexibly-chosen LP antenna system is preferred in wireless communications. An interesting low-profile slot-based cavity antenna was presented in [33] to generate an arbitrarily inclined LP. This LP flexibility is attained by adjusting the energy distribution on the four slots etched on a TE_{220}-mode

Manuscript received XXX. *(Corresponding author: Geng-Bo Wu)*

S.-L. Chen and Y. J. Guo are with the Global Big Data Technologies Centre (GBDTC), University of Technology Sydney (UTS), Ultimo, NSW 2007, Australia. (E-mail: Shulin.Chen@uts.edu.au)

G.-B. Wu, H. Wong, B. J. Chen, and C. H. Chan are with the State Key Laboratory of Terahertz and Millimeter Waves, Department of Electrical Engineering, City University of Hong Kong (CityU), Hong Kong. (E-mail: bogwu2@cityu.edu.hk)

cavity. One finds that this flexible-LP unit (TE_{220}-mode cavity) occupies a large size of $0.9\lambda_0 \times 0.9\lambda_0$, and its impedance bandwidth is narrow, less than 1.0%. It remains a challenge to have a low-profile, wideband, compact slot-based cavity antenna with a flexibly-chosen LP inclination angle.

Notably, one can properly rotate the slot-based cavity antenna to achieve the specified LP inclination angle. Theoretically, the method is simple and does not cause any performance degradation. Nevertheless, the antenna itself must be positioned in a rotated configuration. This may cause issues in practical applications. First, the rotation will change pattern beamwidth in a specific elevational cutting plane, assuming the antenna main beam is directed towards +z-axis. Consequently, the 45° rotated antennas will always have equal beamwidths in the ϕ = 0° and 90° planes, and they can't be deployed for the automotive antenna systems that desire different beamwidths [34]. Furthermore, it will occupy a larger space for the array that employs physically rotated antenna as the element. Take the generation of ±45° LP patterns as an example, one may find it difficult to arrange two physically-rotated antennas compactly [35]. Finally, the rotation will usually cause large variations for the main beam shape and sidelobe levels in the practical environment. As a consequence, the system performance may not be stable.

In this paper, an mm-wave TE_{710}-mode slot-based cavity antenna integrated with a closely-spaced single-layer patch surface is developed to radiate a broadside beam with a flexibly-chosen LP inclination angle. The patch surface is composed of a number of appropriately-rotated C-shaped patches, each being located on top of each slot etched on the cavity surface. The C-shaped patch acts as the polarization conversion surface for each slot radiation, whose polarization is originally directed along $\phi = 90°$. A systematic analysis as well as design guideline is illustrated and provided. Three subsequent surface-integrated antenna prototypes were fabricated and measured that successfully radiate the specified $\phi = 15°$, 45°, and 75°-LP beams, respectively.

This work focuses on providing a generalized polarization-conversion technique for the slot-based cavity antennas. This technique can convert the LP direction of the slot's radiation to a specified inclination angle. There are three main innovations involved in this work. First, to address the limited polarization direction radiated from the slot-based cavity antennas, a single-layer substrate-suspended patch surface is introduced to flexibly choose its far-field polarization angle. The substrate is directly attached onto the slot-based cavity, which facilitates a low-profile, compact integrated system. This surface-integrated system of the exampled TE_{710}-mode slot-based cavity antenna achieves a flexibly-chosen LP direction from $\phi = 15°$ to 165°. Second, the identical C-shaped patch is utilized for each slot's polarization conversion without the use of the inclined slot or non-identical element loading. The polarization-conversion analysis of the TE_{710}-mode slot-based cavity antenna can then be simplified to use an extracted unit cavity, i.e., a TE_{110}-mode single-slot cavity. Consequently, one can predict and optimize the LP performance of the original cavity antenna by investigating this unit cavity antenna. Finally, the developed C-shaped polarization conversion surface along with the unit

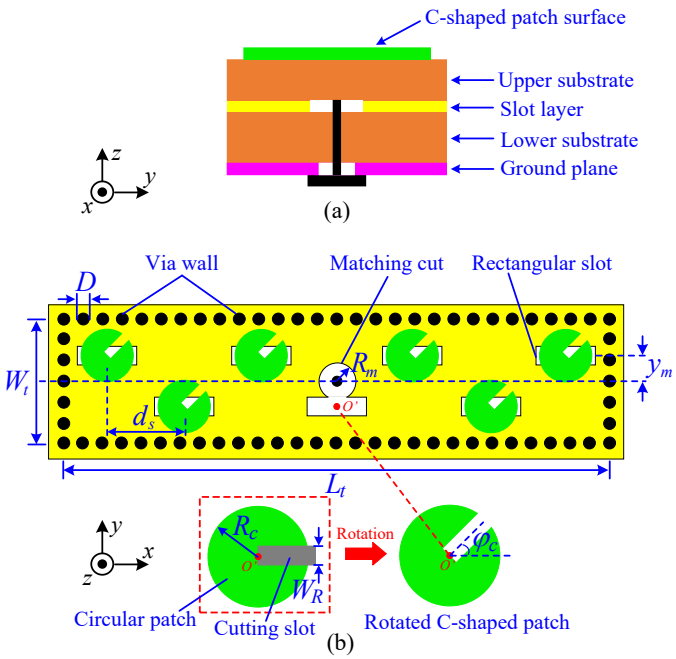

Fig. 1. TE_{710}-mode cavity antenna integrated with C-shaped patch surface. (a) Side view. (b) Top view (For visual purposes, the substrates are not presented and the center C-shaped patch is separately shown).

cavity analysis method can be easily generalized to cavities with different resonant modes. In comparison to properly rotating the antenna for a specified LP state, the developed method utilizes an additional substrate-suspended polarization-conversion surface. It avoids physical rotations for the antenna, which substantially benefits practical applications. The cost is that the additional surface increases antenna complexity and may cause performance degradation.

II. TE_{710}-Mode Cavity Antenna with C-Shaped Patch Surface

A C-shaped patch surface is integrated and attached onto a base TE_{710}-mode cavity antenna to convert its far-field LP direction. Usually, the polarization conversion surface/polarizer is positioned at far-field from the source antenna, and reflection/transmission coefficients are monitored to investigate its polarization conversion. In contrast, our polarization conversion surface is closely-spaced to the base TE_{710}-mode cavity antenna for a low-profile system. This TE_{710} resonant mode is produced with a coaxial feed in a substrate-integrated cavity. Note that the TE_{710}-mode cavity is only exampled to validate our developed LP conversion surface, which can be easily generalized and applied in cavities with different resonant modes.

A. Antenna Configuration

Figs. 1 (a) and (b), respectively, show the side and top views of the TE_{710}-mode slot-based cavity antenna integrated with a patch surface. It consists of two substrates sandwiched by three metallic layers, i.e., the ground plane, the slot layer, and the C-shaped patch surface. Both the lower and upper substrates

are chosen as Rogers 5880 with dielectric constant ε_r = 2.2 and loss tangent $\tan\delta$ = 0.0009. The heights of the lower and upper substrates are 1.575 and 0.787 mm, respectively. A TE_{710}-mode slot-based substrate-integrated cavity antenna is employed as the base configuration. The resonant cavity is formed by the slot layer, the ground plane, and a large number of closely-spaced vias with a diameter of D = 0.3 mm. These vias short the slot layer and the ground plane, and act as PEC walls for the cavity. The length and width of the via wall are L_t = 32 mm and W_t = 4.2 mm, respectively. A coaxial feed is centrally located to excite the TE_{710} cavity mode. The inner probe of the coaxial feed is fully inserted into the lower substrate and its outer conductor is connected to the bottom ground plane. Fig. 2 shows the E-fields excited in the base resonant cavity at 35 GHz. One observes a resonant TE_{710} mode is produced, i.e., there are seven half-wavelength subsections along x-axis, and one half-wavelength subsection along y-axis.

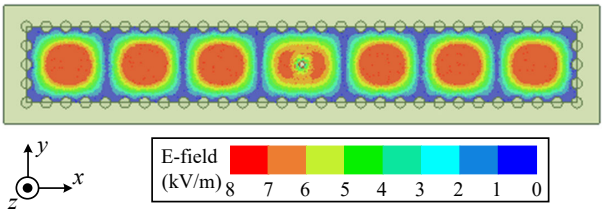

Fig. 2. Top view of the E-fields excited by the co-axial feed in the base cavity without the etched slots.

On the slot layer, seven slots are etched with a uniform distance of d_s along x-axis, each slot being located on one half-wavelength subsection of the TE_{710}-mode wave. Two adjacent slots have opposite offsets along y-axis. This opposite offset is used to compensate for the out-of-phase E-fields between these two adjacent subsections. The offset distance is denoted by y_m. The C-shaped patch surface consists of seven identical rotated C-shaped patches, each being centrally located on top of one corresponding slot. Note that the C-shaped patch located above the center slot is separately shown for visual purposes. As observed from Fig. 1 (b), this C-shaped patch is attained by cutting a rectangular slot from the center of a circular patch and, then, rotated by an angle of φ_c in the xy plane, where φ_c is defined as an azimuthal angle with respect to the +x-axis. The patch's radius is R_c and the cutting slot's width is W_R. The rotated C-shaped patch facilitates the polarization conversion for each slot's radiation. Notice that a circular matching cut with a radius of R_m is centrally etched on the slot layer when the TE_{P10}-mode cavity (P is an integer and $P \geq 2$) has an odd value of P. If P is an even number, the matching cut is positioned on the x-axis with an offset of $d_s/2$ to the center of the slot layer. The matching cut is used for impedance matching between the coaxial feed and the slot-based cavity antenna [12].

B. Polarization Conversion Analysis Using Unit Cavity Antenna

A single rotated C-shaped patch is located above one corresponding slot on the TE_{710}-mode cavity antenna for its polarization conversion. All the C-shaped patches as well as the slots are identical. In this way, the surface-integrated TE_{710}-mode slot-based cavity antenna can be regarded as a seven-element linear array of the unit cavity antenna, i.e., a TE_{110}-mode single-slot cavity integrated with a C-shaped patch. The analysis of the TE_{710}-mode slot-based cavity antenna is then simplified to that of the unit cavity antenna. Fig. 3 shows the configuration of the unit cavity antenna. A coaxial feed is centrally located; its inner probe is inserted into the lower substrate, and its outer conductor is connected to the ground plane. It should be pointed out that the unit cavity antenna is not assigned with periodic boundary conditions (PBCs) due to the staggered layout of the slots and C-shaped patches in the original surface-integrated TE_{710}-mode cavity antenna. The PBC would cause erroneous mutual coupling effects in the unit analysis. In contrast, four vertical perfect electric conductor (PEC) walls are assigned on the lower substrate to form the resonant TE_{110}-mode wave. It is equivalent to a half-wavelength subsection of the TE_{710}-mode cavity, as shown in Fig. 2. The PEC boundaries are used to approximately represent the close-to-zero E-fields at the edges of each half-wavelength subsection. The top view of the unit cavity antenna is shown in Fig. 4. The width W_e and length L_e of the unit cavity should satisfy: $W_e = W_t$, and $L_e = d_s$. A single rectangular slot with a width W_s and a length L_s is etched on its slot layer. The C-shaped patch is located on top of the rectangular slot, and it is separately shown for visual purposes.

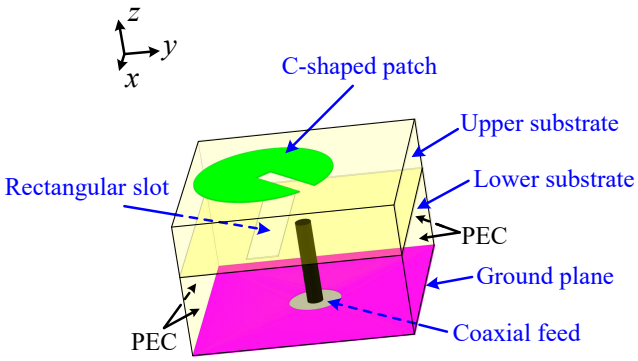

Fig. 3. Overall view of the unit cavity antenna. The substrates are set as transparent for visual purposes.

It is known that the radiated co-pol tangential E-fields of the rectangular slot are directed along the y-axis, being labeled as $\vec{E}_0$. To ease the analysis on the polarization conversion, $\vec{E}_0$ is decomposed into two orthogonal components $\vec{E}_H$ and $\vec{E}_T$, which are directed along the x'- and y'-axis, respectively. The $x'y'$ coordinate is built with a rotation angle of φ_c to the global xy coordinate. One can easily obtain:

$$\begin{aligned} \vec{E}_H &= |\vec{E}_0| \sin\varphi_c \ \hat{e}_{x'} \\ \vec{E}_T &= |\vec{E}_0| \cos\varphi_c \ \hat{e}_{y'} \end{aligned} \tag{1}$$

where $\hat{e}_{x'}$ and $\hat{e}_{y'}$ are respectively the unit vector along $+x'$- and $+y'$-axis.

The rotated C-shaped patch can then be regarded as being excited by the two orthogonal components $\vec{E}_H$ and $\vec{E}_T$. As

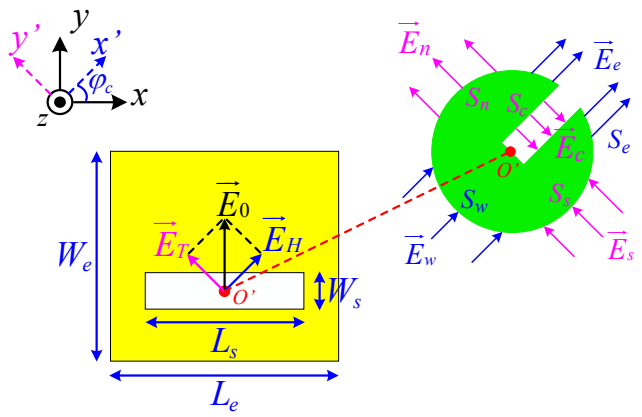

Fig. 4. Top view of unit cavity antenna. The C-shaped patch is separately shown for visual purposes.

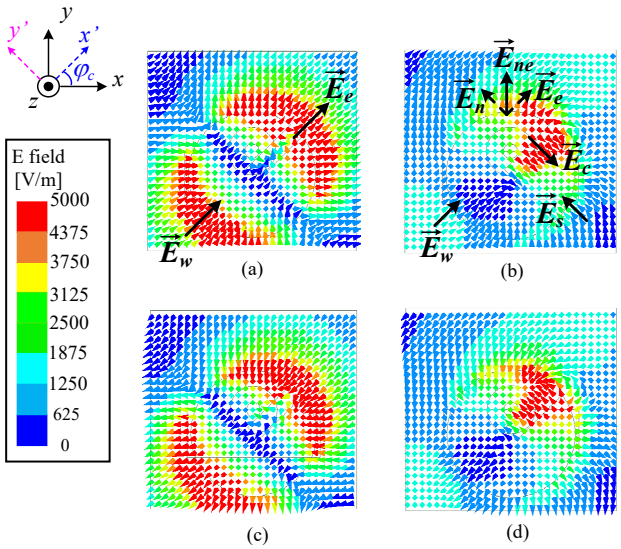

Fig. 5. Top view of the tangential E-fields just above the patch at four time snapshots separated by a quarter period at 34.5 GHz. (a) t = 0. (b) t = T/4. (c) t = T/2. (d) t = 3T/4.

shown in the right of Fig. 4, when $\vec{E}_H$ is considered, a pair of two main tangential E-fields $\vec{E}_w$ and $\vec{E}_e$ are produced along the x'-axis due to the edge coupling between the rotated C-shaped patch and the slot layer. Similarly, a pair of edge coupled fields $\vec{E}_n$ and $\vec{E}_s$ are produced when $\vec{E}_T$ is the source excitation. Meanwhile, another field component $\vec{E}_c$ is obtained between the edges of the cutting slot. One finds that the pair of edge coupled fields $\{\vec{E}_w, \vec{E}_e\}$ or $\{\vec{E}_n, \vec{E}_s\}$ are always directed along the same direction at a snapshot. To achieve a composite co-pol E-fields along $\phi = \varphi_c$, the field component $\vec{E}_c$ should be directed opposite to that of the $\vec{E}_n$ or $\vec{E}_s$. Moreover, these E-fields components should satisfy:

$$\iint_{S_c} \vec{E}_c \times d\vec{s} + \iint_{S_n} \vec{E}_n \times d\vec{s} + \iint_{S_s} \vec{E}_s \times d\vec{s} = 0 \quad (2)$$

$$\iint_{S_e} \vec{E}_e \times d\vec{s} + \iint_{S_w} \vec{E}_w \times d\vec{s} \neq 0 \quad (3)$$

where S_{tt} is the distribution aperture of the corresponding field E_{tt}, and $tt \in \{c, n, s, e, w\}$. The vector element of area $d\vec{s}$ is normal to the surface and directed outward. It is inferred from (2) that far-field radiation contribution of $\vec{E}_c$ over its aperture S_c at the broadside direction cancels out with the sum of the contributions of $\vec{E}_n$ over S_n and $\vec{E}_s$ over S_s for a low x-pol level. Accordingly, those associated parameters, i.e., the C-shaped patch radius R_c and the cutting slot width W_R are critical for optimizing the x-pol level. Furthermore, (3) informs us that the sum of the field $\vec{E}_e$ over S_e and $\vec{E}_w$ over S_w contributes to the co-pol components in the far-field radiations, and hence the sum value must not be zero for effective radiations, i.e., φ_c should not be 0° or 180°. Moreover, the co-pol direction is the same with that of $\vec{E}_e$ or $\vec{E}_w$, which is determined by the source excitation $\vec{E}_H$. As noticed from (1), the direction of $\vec{E}_H$ has an angle of φ_c with respect to the x-axis, indicating that the far-field co-pol direction will be along $\phi = \varphi_c$ at the broadside.

To verify the above analysis, an example is conducted by full-wave simulation of the single-slot cavity antenna integrated with a rotated C-shaped patch. The parameter values (in millimeters) are given in Table I. The C-shaped patch rotation angle φ_c is selected as 45°. It means that the desired co-pol direction would be along ϕ = 45° at the broadside. Fig. 5 shows the top view of the tangential E-fields just above the patch at four time snapshots separated by a quarter period at 34.5 GHz. At t = 0, one observes that there are two main excited tangential E-fields distributed around the top-right and bottom-left edges of the C-shaped patch. All of these tangential E-fields are symmetrically distributed along x'-axis. It is clear that the composite E-fields will be directed along $+x'$-axis, being $\vec{E}_w$ and $\vec{E}_s$ as marked in Fig. 5 (a). At t = T/4, strong E-fields are induced between the edges of the cutting slot, being labeled as $\vec{E}_c$ in Fig. 5 (b). On the other hand, $\vec{E}_s$ produced on the lower edge of the patch has an opposite direction to $\vec{E}_c$. The $\vec{E}_{ne}$ induced on the upper edge can be decomposed into $\vec{E}_n$ and $\vec{E}_e$. One observes that the amplitude of $\vec{E}_c$ is much stronger than that of the $\vec{E}_n$ or $\vec{E}_s$. This agrees with (2) as the aperture S_c is smaller than either S_n or S_s, and the radiation contribution of $\vec{E}_c$ over its aperture S_c at the broadside direction should compensate for the sum of the contributions of $\vec{E}_n$ over S_n and $\vec{E}_s$ over S_s. The composite radiating fields contributed from the $\vec{E}_w$ and $\vec{E}_{w'}$ are directed towards $+x'$-axis. It indicates that the composite far fields are always directed along $+x'$-axis at the broadside in the first half period. Figs. 5 (c) and (d) show the tangential E-fields at two time snapshots in the other half period. The composite fields are always directed along $-x'$-axis at the broadside in the other half period. Clearly, an LP state along ϕ = φ_c (45°) is achieved.

TABLE I
VALUES FOR THE PATCH-INTEGRATED SINGLE-SLOT CAVITY ANTENNA

Parameter	W_e	L_e	R_c	W_R	L_s	W_s	y_m
Values (mm)	4.2	4.35	1.325	0.35	2.8	1	0.5

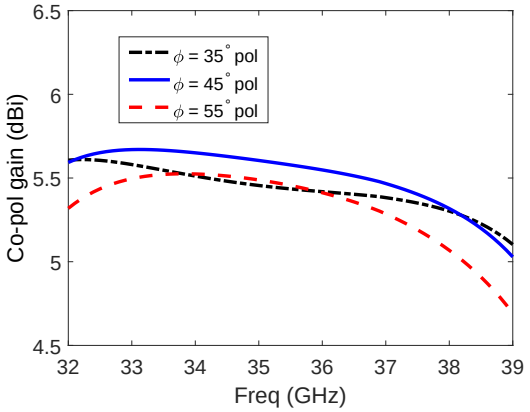

(a)

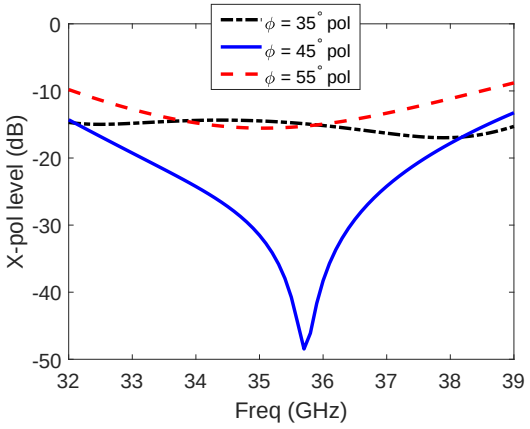

(b)

Fig. 6. Simulated broadside gains as a function of the source frequency. (a) Co-pol gain. (b) X-pol level.

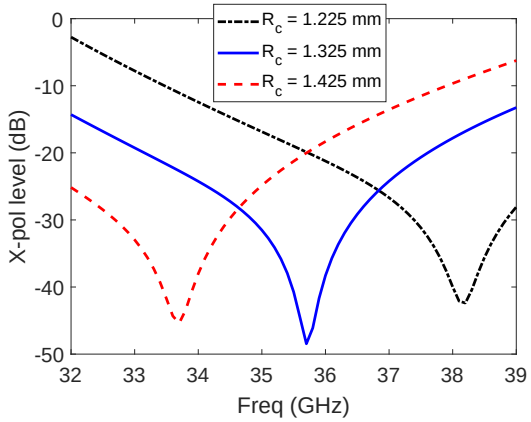

Fig. 7. X-pol levels of the 45°-pol patch-integrated unit cavity antenna when the C-shaped patch radius R_c is varied.

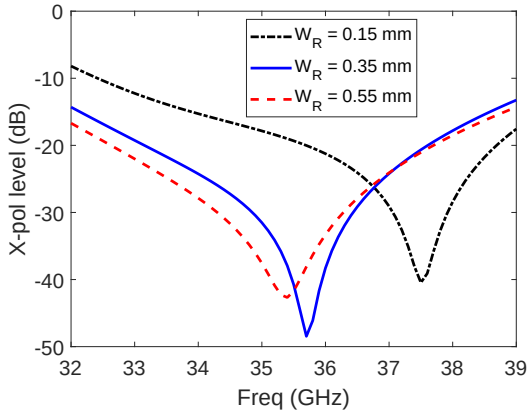

Fig. 8. X-pol levels of the 45°-pol patch-integrated unit cavity antenna when the width of the cutting slot W_R is varied.

As known from the definition of antenna's polarization [36], [37], one can determine the LP direction based on the obtained co-pol gain and x-pol level in a specified cutting plane for the single-slot patch-integrated cavity antenna. Assume the LP direction is along $\phi = \varphi_{co}$, the co-pol and x-pol gains are respectively the θ- and ϕ-components of the total gain in the $\phi = \varphi_{co}$ plane (E-plane). X-pol level is the difference between the x-pol and co-pol gains. Figs. 6 (a) and (b) respectively show the co-pol gains and x-pol levels as functions of the source frequency in the E-planes when the assumed co-pol is directed along ϕ = [35°, 45°, 55°]. One observes that in the frequency band from 33 to 38 GHz, the gain is highest and the x-pol level is the lowest for the ϕ = 45°-pol. It validates a successful polarization conversion from the ϕ = 90°-pol of the base slot radiation to the desired ϕ = 45°-pol. It should be pointed out that the LP performance of the antenna can also be verified by exploiting the antenna axial ratios (ARs).

C. Parameter Study

It is previously acknowledged that the C-shaped rotation angle (φ_c) determines the patch-integrated cavity antenna's far-field LP angle. If a flexibly-chosen LP inclination angle is desired, one should choose the corresponding value of φ_c. At this $\phi = \varphi_c$ polarization state, two important parameters, i.e., the patch radius R_c and the cutting slot width W_R, are studied for the desired low-x-pol performance at a specific operating band.

The above 45°-pol patch-integrated unit cavity antenna is simulated when the C-shaped patch radius R_c is varied among 1.225, 1.325, and 1.425 mm. The x-pol levels as a function of the source frequency are shown in Fig. 7. At a specified frequency such as 33.5 GHz, the x-pol level is the lowest at around -41.7 dB when $R_c = 1.425$ mm. This x-pol level is respectively increased to -10.1 and -21.7 dB when R_c is 1.225 and 1.325 mm. Thus, one can alter R_c to optimize the x-pol level at the specified operating frequency. Furthermore, if one considers the x-pol level as a function of the source frequency, when $R_c = 1.425$ mm, it is observed that the x-pol level is lower than -15 dB for the frequency higher than 34.6 GHz. When R_c is reduced to 1.325 mm, the -15-dB x-pol bandwidth ranges from 32.2 to 38.5 GHz. With a further decrease of R_c to be 1.225 mm, the x-pol level is lower than -15 dB for the frequency lower than 36.6 GHz. It is obvious that the LP conversion frequency bandwidth is shifting towards the lower band with an increase of R_c. Fig. 8 shows the x-pol levels of the 45°-pol patch-integrated unit cavity antenna when W_R is varied. The LP conversion frequency bandwidth shifts towards the lower band when W_R is increased from 0.15 to

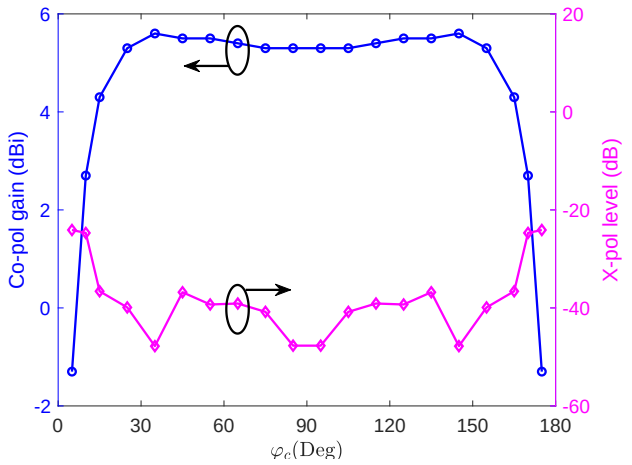

Fig. 9. Simulated co-pol gain and x-pol level for the TE_{110}-mode cavity antenna integrated with a C-shaped patch when φ_c is varied at 34.5 GHz.

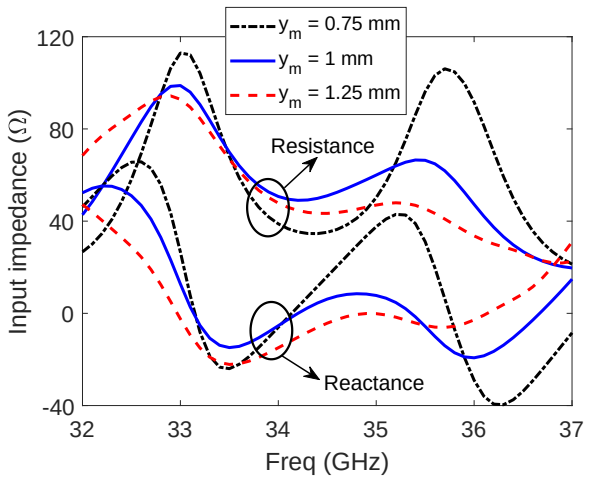

Fig. 10. Input impedance of the 45°-pol surface-integrated TE_{710}-mode cavity antenna when y_m is varied.

0.35 mm. With a further increase to 0.55 mm, the band shift becomes small. It is concluded that one may also vary W_R to control the LP conversion bandwidth.

With the well-optimized low-x-pol levels, one then needs to consider the gain behaviors when the LP angle is varied. Again, the TE_{110}-mode single-slot unit cavity antenna is utilized for the analysis. Fig. 9 shows the obtained co-pol gain and x-pol level at the broadside when φ_c is varied from 5° to 175° at 34.5 GHz. The x-pol levels are low, below –20 dB, for all φ_c values. When φ_c is 5°, the gain is only −1.3 dBi. The gain is greatly improved to 5.6 dBi when φ_c increases to 35°. Then, the gain has only 0.3-dBi variation when φ_c is further increased to 85°. One finds that the gain curve is symmetrical with 90°. This is because for any two supplementary values of φ_c, their corresponding antenna configurations are symmetrical with y-axis. It is predicted that to achieve an accepted gain performance for the TE_{710}-mode antenna, the antenna's LP angle should be varied among $\phi = 15°$ to 165°.

D. Antenna Impedance Analysis

Concerning impedance characteristics, the unit behaviors are quite different from that of the final TE_{710}-mode cavity antenna. This is because the ideal PEC boundaries used in the unit analysis change its original impedance condition that has mutual couplings from the other half-wavelength subsections in the TE_{710}-mode cavity. Therefore, the impedance analysis is conducted for the surface-integrated TE_{710}-mode cavity antenna rather than the unit cavity antenna.

Based on the previous polarization analysis for the unit cavity antenna, one can form a surface-integrated TE_{710}-mode cavity antenna using the determined values of the parameters φ_c, R_c, and W_R for a desired LP state. The parameters, including the slot offset y_m, the slot length L_s, the slot width W_s, and the matching cut R_m, are optimized for impedance matching. For example, a parameter study was conduced on the slot offset y_m as shown in Fig. 10. When y_m = 0.75 mm, a large variation of the resistance and reactance as a function of the frequency is observed, and hence the impedance bandwidth is narrow. When y_m is increased to be 1 mm, at the desired frequency band from 33 to 36.5 GHz, both curves of the resistance and reactance become much flatter. Moreover, their values are close to 50 Ω and 0 Ω, respectively. Hence, good impedance matching is achieved in this band. The input impedance has relatively small changes with a further increase of y_m = 1.25 mm,. The final design selects y_m as 1 mm considering the overall impedance matching, x-pol levels, and realized gains. The optimized values (in millimeters) for other parameters are: L_s = 4.3, W_s = 0.8, and R_m = 0.9. In this impedance-optimization process, the x-pol level of the surface-integrated TE_{710}-mode cavity antenna is sacrificed. One could facilitate fine-tuning for the parameters R_c and W_R to improve x-pol levels, while the antenna impedance would be slightly changed. Additional parameter adjustments are then required to balance the x-pol and impedance matching.

Furthermore, the rotation angle φ_c has a large effect on the antenna impedance. It can be inferred that the near-field coupling between the C-shaped patch and the slotted cavity will have noticeable changes with the variation of φ_c. One can vary φ_c to achieve a different LP state, while other parameters should be re-optimized to make the impedance matched.

III. Performance and Discussion

A. Simulated and Measured Results

With the optimized parameter values, the surface-integrated TE_{710}-mode cavity antenna in Fig. 1 is simulated by HFSS. Fig. 11 shows the obtained x-pol levels when the assumed co-pol is directed long $\phi = \{35°, 45°, 55°\}$. It is clear that the lowest x-pol value is obtained for $\phi = 45°$ pol for the frequency from 32.5 to 37 GHz, i.e., a co-pol along ϕ = 45° is obtained. This verifies the effectiveness of the polarization analysis using the unit cavity antenna. In comparison to the x-pol level of the unit cavity antenna shown in Fig. 6(b), the x-pol of the 45°-pol TE_{710}-mode cavity antenna is a bit worse. This is caused by the mutual coupling effect and the sacrifice in parameter optimizations required for the impedance matching.

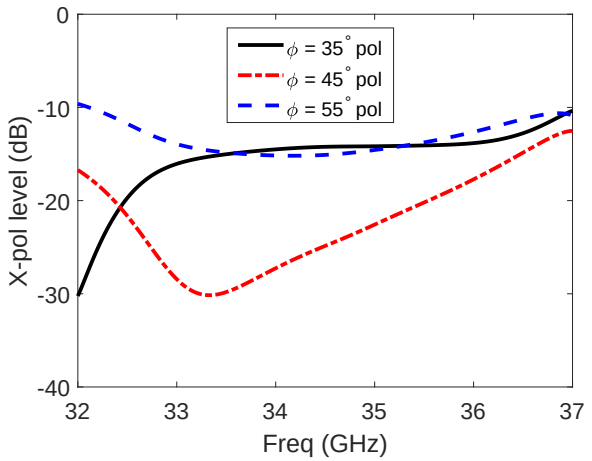

Fig. 11. Simulated x-pol levels for the surface-integrated TE_{710}-mode cavity antenna.

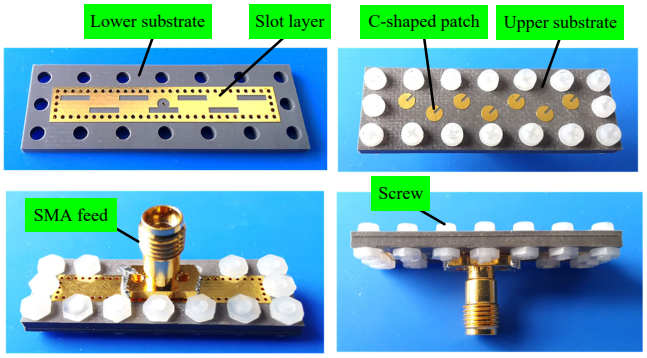

Fig. 12. The fabricated prototype of the 45°-pol surface-integrated TE_{710}-mode cavity antenna before and after assembly.

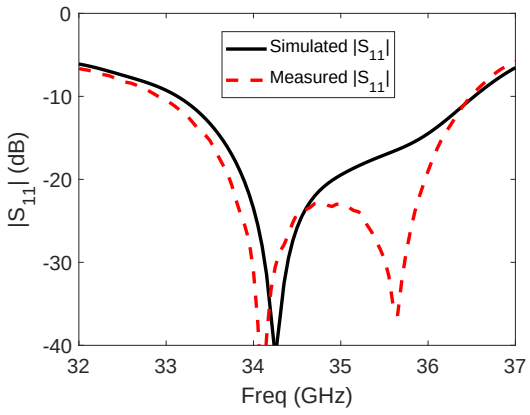

Fig. 13. Simulated and measured S-parameters for the 45°-pol surface-integrated TE_{710}-mode cavity antenna.

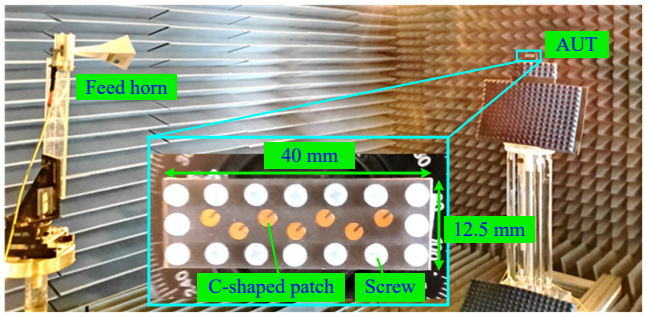

Fig. 14. The fabricated 45°-pol surface-integrated TE_{710}-mode cavity antenna measured with the far-field range system.

Fig. 12 shows the fabricated prototype of the 45°-pol surface-integrated TE_{710}-mode cavity antenna before and after assembly. Note that the probe length of the SMA feed should be equal to the height (1.575 mm) of the lower substrate to maintain a good impedance matching. Using a high-end SMA or metalizing the hole that accommodates the probe can meet this requirement. The latter method is easier and cheaper in practice and is adopted in this work. To facilitate the antenna assembly, the substrate dimensions are increased to include a number of Teflon screws. The antenna is then re-simulated based on the dimensions in the final prototype. Fig. 13 shows its simulated and measured $|S_{11}|$. The simulated -10-dB impedance bandwidth ranges from 33.15 to 36.50 GHz, a 9.6% fractional bandwidth. The measured bandwidth is from 32.95 to 36.50 GHz, agreeing well with the simulated one. Besides the first resonance at around 34.1 GHz, one may observe a second strong resonance at around 35.65 GHz for the measured $|S_{11}|$. As noted from the input impedance shown in Fig. 10, the 45°-pol surface-integrated TE_{710}-mode cavity antenna has two possible strong resonances (zero-reactance points) at around 34.2 and 35.4 GHz, respectively. The simulation did not capture the second resonance due to its resistance value larger than 50 Ω at 35.4 GHz. Nevertheless, this second resonance is observed in the measured $|S_{11}|$. Further investigations indicate that it is probably because the fabrication tolerances lower the resistance value at the resonance frequency.

As illustrated in Fig. 14, the antenna's radiation patterns were measured with the far-field antenna measurement system located at the City University of Hong Kong (CityU). One may observe that the Teflon screws are relatively large with respect to the antenna size. All of the simulated radiation patterns and gains that will be provided later have included the effect of these screws. Further simulations indicate these screws have negligible effects on the co-pol patterns and realized gains of the antenna. They have only a small effect on the broadside x-pol level. Fig. 15 shows the simulated and measured radiation patterns at 34.5 GHz. Good agreement is also observed between them. The measured patterns have a slight shift in the main beam compared with the simulated ones in both E- and H-planes. This may be introduced by the inaccuracy that existed in measurement alignments. The measured 3-dB beamwidth is 21.0° and 18.0° in E- and H-plane, respectively. The measured sidelobe level is around -10 dB, and the x-pol level is around -20.0 dB at the broadside. As for those being interested in the radiation characteristics for communications systems, the radiation patterns in the $\phi = 0°$ and 90° planes were measured and compared. Fig. 16 (a) and (b) show the radiation patterns in the $\phi = 0°$ and 90° planes at 34.5 GHz, respectively. The measured pattern agrees with the simulated one in the $\phi = 0°$ plane. In the $\phi = 90°$ plane, the measurement also has a good agreement with the

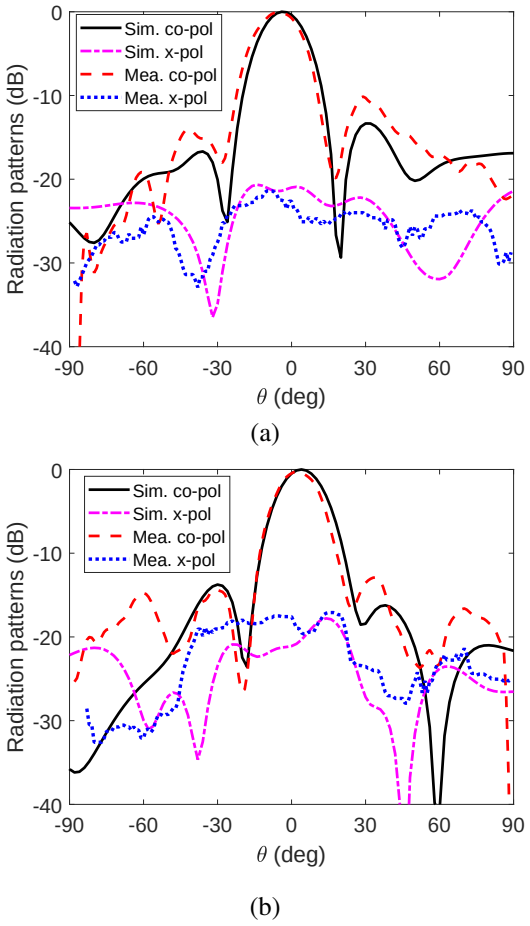

Fig. 15. Simulated and measured radiation patterns for the 45°-pol surface-integrated TE_{710}-mode cavity antenna at 34.5 GHz. (a) E plane (ϕ = 45° plane). (b) H plane (ϕ = 135° plane).

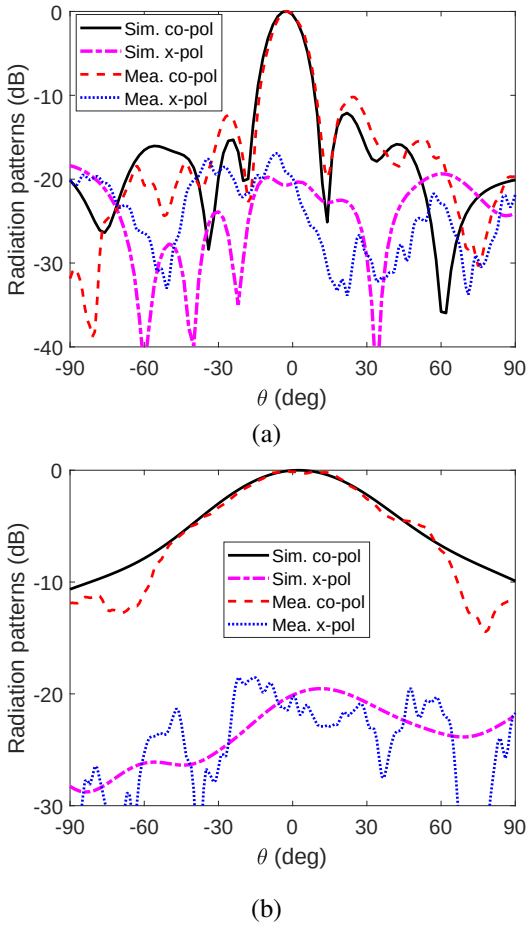

Fig. 16. Simulated and measured radiation patterns for the 45°-pol surface-integrated TE_{710}-mode cavity antenna at 34.5 GHz. (a) ϕ = 0° plane. (b) ϕ = 90° plane.

simulation in the $\pm 50^\circ$ angular range. An obvious drop occurs at around $\theta = \pm 75^\circ$. Given the wide main beam angle in $\phi = 90^\circ$ plane and the angle $\theta = \pm 75^\circ$ being far away from the broadside direction, the drop is probably caused by the mounting platform and fixture used to fix the antenna.

Fig. 17 shows the simulated and measured realized gains as a function of the source frequency. The measured peak value is 14.1 dBi at 35 GHz, which is around 0.5 dB higher than the simulated peak value of 13.6 dBi at 34.5 GHz. This may be because the measured beamwidth becomes slightly narrower given those inaccuracies existed in the measurements. The measured 3-dB gain bandwidth ranges from 33.3 to 36.7 GHz. Considering the impedance and gain bandwidth, the overall operating bandwidth ranges from 33.3 to 36.5 GHz, a 9.2% fractional bandwidth. The measured x-pol level is lower than -12.9 dB across this band. It is worthy of mentioning that the antenna has a negligible beam squint in the operating band due to the inherent property of a resonant cavity. The simulated sidelobe level as a function of the source frequency is shown in Fig. 18. The lowest sidelobe level occurs at 35.25 GHz with a value of –13.7 dB, which is close to the theoretical sidelobe level (–13.5 dB) of a uniform linear array. The sidelobe levels are a bit higher at frequencies lower than 34 GHz within

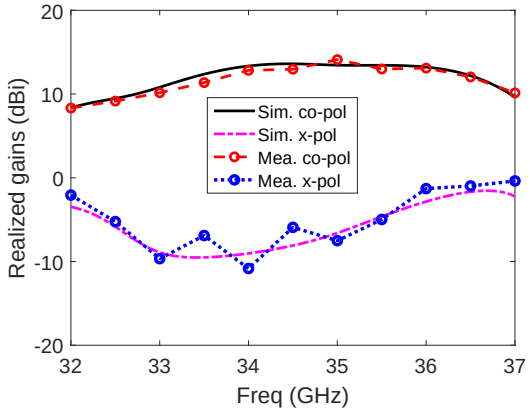

Fig. 17. Simulated and measured co-pol and x-pol realized gains for the 45°-pol surface-integrated TE_{710}-mode cavity antenna.

the operating bandwidth. The increased sidelobe levels are caused by mode impurities at those frequencies being far away from the center one in the base cavity. Fig. 18 also shows the simulated total efficiency as a function of the source frequency. In the operating bandwidth, the efficiency varies between 87.7% and 98.9%. Further investigations show that ohmic losses on the C-shaped patches are negligible with

TABLE II
DETAILED COMPARISON AMONG THE SINGLE-FEED POLARIZATION-CONVERSION SLOT-BASED CAVITY ANTENNAS

Antennas	Pol.	Technique	Element number	IBW (GHz)	3-dB GBW (GHz)	OFBW (%)	-15-dB XBW (GHz)	PRG (dBi)	PTE (%)	Antenna size ($\lambda_0 \times \lambda_0$)	Cavity size ($\lambda_0 \times \lambda_0$)	IE	Complexity
[20]	45°	ACIL	16×1	34.07–35.1	34.07–35.1	2.7	N.A.	15.64	71.1	6.99×1.96	6.66×0.40	No	Low
[21]	45°	SICL	6×5	33.95–34.86	33.95–34.86	2.6	N.A.	17.09	N.A.	5.07×3.82	3.79×3.82	No	High
[22]	45°	DRA	8×1	34.0–36.2	34.3–36	4.8	N.A.	13.55	85.0*	8.42×6.35	6.47×0.56	Yes	Medium
This work	45°	CSP	7×1	32.95–36.5	33.3–36.7	9.2	32.7–35.9	14.1	98.9*	4.65×1.6	3.74×0.49	Yes	Low
	45°	CSP	7×5	33.2–34.9*	33.1–34.4*	3.6*	32.5–35.8*	19.5*	97.9*	4.65×3.34	3.74×2.45	Yes	Low
	15°	CSP	7×1	32.85–36.1	33.0–36.7	9.0	33.6–35.6*	14.6	97.3*	4.65×1.6	3.74×0.49	Yes	Low
	75°	CSP	7×1	32.7–36.1	32.8–36.7	9.6	32–37	13.7	96.4*	4.65×1.6	3.74×0.49	Yes	Low

ACIL: Alternative conductive and inductive loading; SICL: Substrate integrated coaxial line; DRA: Dielectric resonant antenna; CSP: C-shaped patch; IBW: Impedance bandwidth; GBW: Gain bandwidth; OFBW: Overlapped fractional bandwidth; XBW: X-pol bandwidth; PRG: Peak realized gain; PTE: Peak total efficiency; IE: Identical element; N.A.: Not available; * indicates the data obtained through simulation.

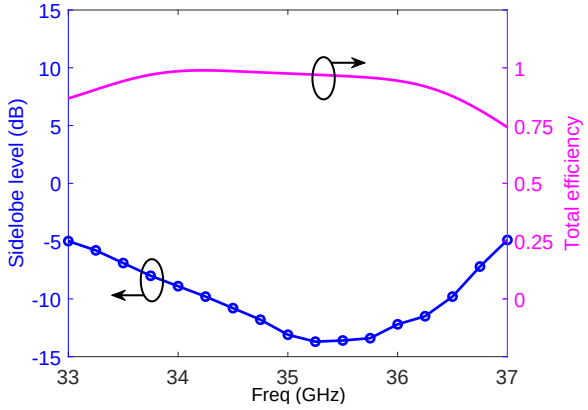

Fig. 18. Simulated sidelobe level and total efficiency for the 45°-pol surface-integrated TE_{710}-mode cavity antenna.

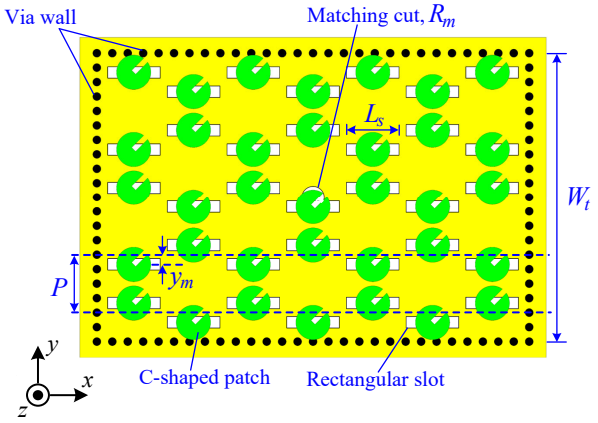

Fig. 19. Top view of the 45°-pol surface-integrated TE_{750}-mode cavity antenna. The substrates are not shown for visual purposes.

respect to antenna gain.

B. Discussion

Table II gives a detailed comparison between those reported 45°-LP slot-based cavity antennas and our developed antennas. All of the antennas are operating at mm-wave band, have a single feed without utilizing a complex power distribution network. To achieve an impedance-matched, high-gain 45°-LP slot-based cavity antennas, several techniques have been presented, including the alternative capacitive and inductive loaded slots (ACIL) [20], the substrate integrated coaxial line (SICL) [21], the dielectric resonant antenna (DRA) loading [22], and the C-shaped patch (CSP) loading developed in this work. As observed from the comparison table, all of these previously reported antennas did not provide an x-pol bandwidth. A –15-dB x-pol bandwidth for our developed antennas is chosen as a reference for future readers. This x-pol limit is sufficient for targeted applications in mm-wave imaging systems [38], [39]. One could choose the desired x-pol limit depending on the requirements. If a more ambitious x-pol level is targeted, the antenna bandwidth could be reduced. The overlapped fractional bandwidth (OFBW) overlaps the impedance-matching bandwidth and the 3-dB gain bandwidth only, i.e., the x-pol bandwidth is not included. One finds that the 45°-pol surface-integrated slot-based cavity antenna developed in this work outperforms those reported antennas considering the overall performance characteristics, including the OFBW, the gain values, and the design and fabrication complexity.

To examine the developed polarization-conversion technique in a full-corporate array, we have considered a 45°-pol surface-integrated TE_{750}-mode cavity antenna, i.e., the element number is 7×5. Its top view is shown in Fig. 19. The offset y_m is facilitated for two adjacent slots in the same column/row to compensate for the out-of-phase E-fields produced by the two corresponding half-wavelength subsections in the cavity. The antenna parameter values (in millimeters) are optimized as: $W_t = 21$, $P = 4.2$, $L_s = 4$, $y_m = 0.65$, $R_c = 1.375$. The other parameter values remain the same as in Table I. Fig. 20 shows the obtained $|S_{11}|$ and realized gains for the 45°-pol surface-integrated TE_{750}-mode cavity antenna. The

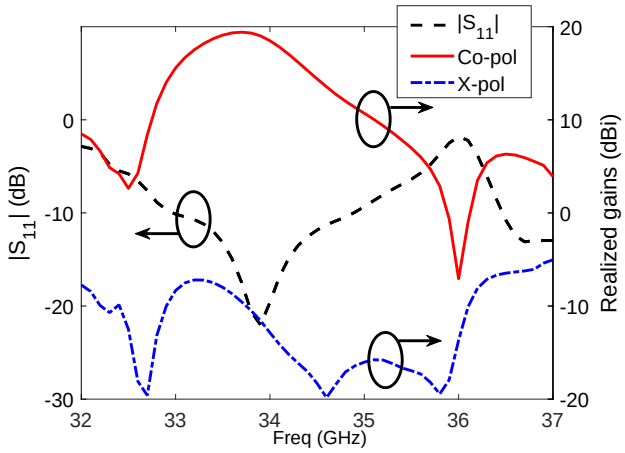

Fig. 20. Simulated $|S_{11}|$ and realized gains for the 45°-pol surface-integrated TE_{750}-mode cavity antenna.

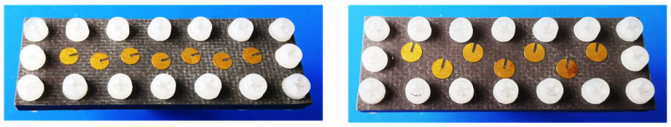

Fig. 21. The fabricated antenna prototypes. (a) The 15°-pol surface-integrated TE_{710}-mode cavity antenna. (b) The 75°-pol surface-integrated TE_{710}-mode cavity antenna.

simulated –10-dB impedance bandwidth ranges from 33.2 to 34.9 GHz, and the 3-dB gain bandwidth is from 33.1 to 34.4 GHz. The overlapped bandwidth is thus from 33.2 to 33.4 GHz, i.e., a fractional bandwidth of 3.6%. The x-pol level is lower than –24 dB within this bandwidth. Compared with the antenna with a similar full-corporate array reported in [21], our technique employing the C-shaped patch surface has improved bandwidth and gain using a more compact and simple configuration.

IV. Flexibly-Chosen Linear Polarization

In the following, two more examples of the surface-integrated TE_{710}-mode cavity antenna are conducted to further verify their overall polarization conversion performance.

A. Two Examples

The desired polarization angle for the first surface-integrated TE_{710}-mode cavity antenna is $\phi = 15°$ with φ_c selected as 15°. Several parameter values are updated to achieve a low x-pol level as well as good impedance matching, and their values (in millimeters) are optimized as: L_s = 4.15, W_s = 0.525, d_s = 0.4, W_R = 0.35, and R_m = 1. The other parameters keep the same as the previous study in Section II, and the antenna was simulated using HFSS. An antenna prototype was fabricated and assembled as shown in Fig. 21 (a). Its simulated and measured S-parameters are shown in Fig. 22. The measured $|S_{11}| \leq -10$ dB bandwidth ranges from 32.85 to 36.1 GHz. Fig. 23 shows the broadside simulated and measured co-pol and x-pol realized gains at ϕ = 15°. It is

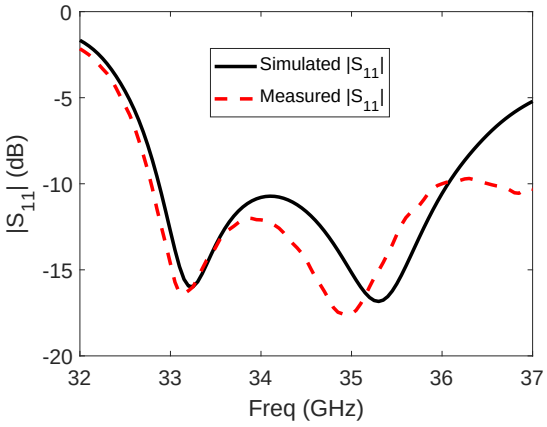

Fig. 22. Simulated and measured S-parameters for the 15°-pol surface-integrated TE_{710}-mode cavity antenna.

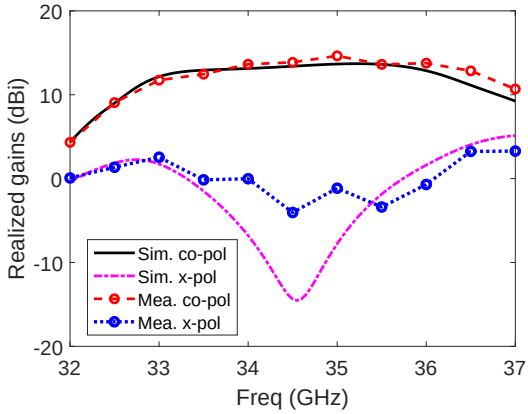

Fig. 23. Simulated and measured co-pol and x-pol realized gains for the 15°-pol surface-integrated TE_{710}-mode cavity antenna.

obvious that an LP state along ϕ = 15° is achieved. The measured peak realized gain is 14.6 dBi at 35 GHz, and the 3-dB gain bandwidth is from 33.0 to 36.7 GHz. The overlapped impedance and gain bandwidth ranges from 33.0 to 36.1 GHz, a 9.0% fractional bandwidth. The simulated total efficiency varies between 91.5% and 97.3% within this band. The simulated -15-dB x-pol bandwidth ranges from 33.6 to 35.6 GHz, and the measured x-pol level is less than –13.5 dB.

The second example is to realize a 75°-pol radiation, i.e., φ_c = 75°. Those updated parameter values (in millimeters) are: L_s = 4.3, W_s = 0.6, d_s = 1.2, R_c = 1.45, and R_m = 1.2. Fig. 21 (b) shows a photo of the assembled antenna prototype. Its simulated and measured S-parameters are shown in Fig. 24. The measured $|S_{11}| \leq -10$ dB bandwidth ranges from 32.7 to 36.1 GHz, a 9.9% fractional bandwidth. Fig. 25 shows the broadside simulated and measured co-pol and x-pol realized gains at ϕ = 75°. The measured peak gain value is 13.7 dBi at 35.5 GHz, and the 3-dB gain bandwidth is from 32.8 to 36.7 GHz. The measured x-pol level is lower than −18.0 dB in the frequency band from 32.8 to 36.1 GHz. The simulated total efficiency is varied between 85.1% and 96.4% within this band.

Performance characteristics of the three fabricated TE_{710}-mode cavity antenna prototypes have been included and

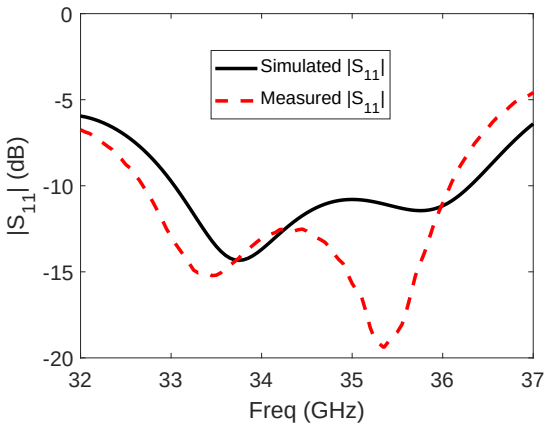

Fig. 24. Simulated and measured S-parameters for the 75°-pol surface-integrated TE_{710}-mode cavity antenna.

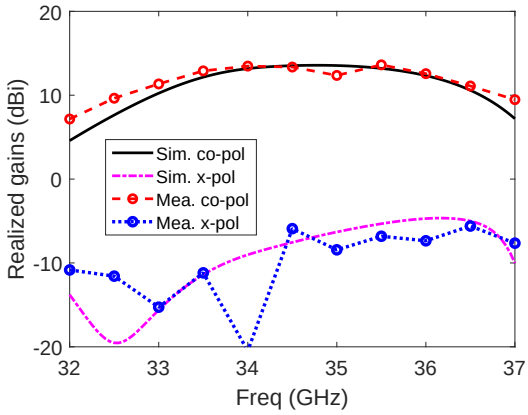

Fig. 25. Simulated and measured co-pol and x-pol realized gains for the 75°-pol surface-integrated TE_{710}-mode cavity antenna.

compared in Table II. One finds that all these three antennas achieve a similar overlapped impedance and 3-dB gain bandwidth. Moreover, all of them achieve a very high total efficiency, i.e., the simulated peak efficiencies are higher than 95%. Their peak realized gains have less than 1 dB difference. Concerning the x-pol behaviors, the –15-dB x-pol bandwidth has an obvious enhancement when φ_c is increased from 15° to 75°.

V. Conclusion

A closely-spaced C-shaped patch surface was developed to improve the polarization flexibility of the slot-based cavity antennas. A TE_{710}-mode slot-based cavity antenna was initially selected as the basic configuration. It radiates a broadside beam with the co-polarization direction along $\phi = 90°$. A simple yet effective analysis method that uses a single-slot unit cavity antenna was presented to facilitate the polarization conversion analysis. Simulations indicate that the linear polarization direction of the TE_{710}-mode cavity antenna could be flexibly chosen from 15° to 165° with the use of closely-spaced C-shaped patch surface. They were further validated by the fabricated three prototypes, which respectively radiate the specified $\phi = \{15°, 45°, 75°\}$-linear polarization broadside beam. The developed surface-integrated slot-based cavity antennas have a flexibly-chosen LP angle with a low-profile and compact configuration, which can be widely applied in mm-wave wireless communications.

References

[1] X. Bai, S. Qu, S. Yang, J. Hu, and Z. Nie, "Millimeter-wave circularly polarized tapered-elliptical cavity antenna with wide axial-ratio beamwidth," *IEEE Trans. Antennas Propag.*, vol. 64, no. 2, pp. 811–814, 2016.

[2] Q. Zhu, K. B. Ng, C. H. Chan, and K.-M. Luk, "Substrate-integrated-waveguide-fed array antenna covering 57–71 GHz band for 5G applications," *IEEE Trans. Antennas Propag.*, vol. 65, no. 12, pp. 6298–6306, 2017.

[3] O. Quevedo-Teruel *et al.*, "Glide-symmetric fully metallic Luneburg lens for 5G communications at Ka-band," *IEEE Antennas Wireless Propag. Lett.*, vol. 17, no. 9, pp. 1588–1592, 2018.

[4] S. Alkaraki *et al.*, "Compact and low-cost 3-D printed antennas metalized using spray-coating technology for 5G mm-wave communication systems," *IEEE Antennas Wireless Propag. Lett.*, vol. 17, no. 11, pp. 2051–2055, 2018.

[5] M. Chen, A. Epstein, and G. V. Eleftheriades, "Design and experimental verification of a passive Huygens' metasurface lens for gain enhancement of frequency-scanning slotted-waveguide antennas," *IEEE Trans. Antennas Propag.*, vol. 67, no. 7, pp. 4678–4692, 2019.

[6] H. Xu, J. Zhou, K. Zhou, Q. Wu, Z. Yu, and W. Hong, "Planar wideband circularly polarized cavity-backed stacked patch antenna array for millimeter-wave applications," *IEEE Trans. Antennas Propag.*, vol. 66, no. 10, pp. 5170–5179, 2018.

[7] J. Park, M. Choo, S. Jung, D. Choi, J. Choi, and W. Hong, "A software-programmable directivity, beamsteering, and polarization reconfigurable block cell antenna concept for millimeter-wave 5G phased- array architectures," *IEEE Trans. Antennas Propag.*, vol. 69, no. 1, pp. 146–154, 2021.

[8] Q. Yang *et al.*, "Cavity-backed slot-coupled patch antenna array with dual slant polarization for millimeter-wave base station applications," *IEEE Trans. Antennas Propag.*, vol. 69, no. 3, pp. 1404–1413, 2021.

[9] D. Kim, M. Zhang, J. Hirokawa, and M. Ando, "Design and fabrication of a dual-polarization waveguide slot array antenna with high isolation and high antenna efficiency for the 60 GHz band," *IEEE Trans. Antennas Propag.*, vol. 62, no. 6, pp. 3019–3027, 2014.

[10] M. Ferrando-Rocher, J. I. Herranz-Herruzo, A. Valero-Nogueira, B. Bernardo-Clemente, A. U. Zaman, and J. Yang, "8×8 Ka-band dual-polarized array antenna based on gap waveguide technology," *IEEE Trans. Antennas Propag.*, vol. 67, no. 7, pp. 4579–4588, 2019.

[11] Q. Yang *et al.*, "Dual-polarized crossed slot array antenna designed on a single laminate for millimeter-wave applications," *IEEE Trans. Antennas Propag.*, vol. 68, no. 5, pp. 4120–4125, 2020.

[12] W. Han, F. Yang, J. Ouyang, and P. Yang, "Low-cost wideband and high-gain slotted cavity antenna using high-order modes for millimeter-wave application," *IEEE Trans. Antennas Propag.*, vol. 63, no. 11, pp. 4624–4631, Nov. 2015.

[13] M. Asaadi and A. Sebak, "High-gain low-profile circularly polarized slotted SIW cavity antenna for MMW applications," *IEEE Antennas Wireless Propag. Lett.*, vol. 16, pp. 752–755, 2017.

[14] H. Irie and J. Hirokawa, "Perpendicular-corporate feed in three-layered parallel-plate radiating-slot array," *IEEE Trans. Antennas Propag.*, vol. 65, no. 11, pp. 5829–5836, 2017.

[15] J. Liu, A. Vosoogh, A. U. Zaman, and J. Yang, "A slot array antenna with single-layered corporate-feed based on ridge gap waveguide in the 60 GHz band," *IEEE Trans. Antennas Propag.*, vol. 67, no. 3, pp. 1650–1658, 2019.

[16] Q. Yuan, Z. Hao, K. Fan, and G. Q. Luo, "A compact W-band substrate-integrated cavity array antenna using high-order resonating modes," *IEEE Trans. Antennas Propag.*, vol. 66, no. 12, pp. 7400–7405, 2018.

[17] Y. W. Wu, Z. C. Hao, and Z. W. Miao, "A planar W-band large-scale high-gain substrate-integrated waveguide slot array," *IEEE Trans. Antennas Propag.*, vol. 68, no. 8, pp. 6429–6434, 2020.

[18] K. Wu, Y. J. Cheng, T. Djerafi, and W. Hong, "Substrate-integrated millimeter-wave and terahertz antenna technology," *Proc. IEEE*, vol. 100, no. 7, pp. 2219–2232, 2012.

[19] D. Kim, W. Chung, C. Park, S. Lee, and S. Nam, "A series slot array antenna for 45°-inclined linear polarization with SIW technology," *IEEE Trans. Antennas Propag.*, vol. 60, no. 4, pp. 1785–1795, 2012.

[20] ——, "Design of a 45°-inclined SIW resonant series slot array antenna for Ka-band," *IEEE Antennas Wireless Propag. Lett.*, vol. 10, pp. 318–321, 2011.
[21] B. Liu *et al.*, "A 45° linearly polarized slot array antenna with substrate integrated coaxial line technique," *IEEE Antennas Wireless Propag. Lett.*, vol. 17, no. 2, pp. 339–342, 2018.
[22] M. S. Abdallah, Y. Wang, W. M. Abdel-Wahab, and S. Safavi-Naeini, "Design and optimization of SIW center-fed series rectangular dielectric resonator antenna array with 45° linear polarization," *IEEE Trans. Antennas Propag.*, vol. 66, no. 1, pp. 23–31, 2018.
[23] X. Gao, X. Han, W. Cao, H. O. Li, H. F. Ma, and T. J. Cui, "Ultrawideband and high-efficiency linear polarization converter based on double V-shaped metasurface," *IEEE Trans. Antennas Propag.*, vol. 63, no. 8, pp. 3522–3530, 2015.
[24] Q. Zheng, C. Guo, and J. Ding, "Wideband metasurface-based reflective polarization converter for linear-to-linear and linear-to-circular polarization conversion," *IEEE Antennas Wireless Propag. Lett.*, vol. 17, no. 8, pp. 1459–1463, 2018.
[25] A. K. Baghel, S. S. Kulkarni, and S. K. Nayak, "Linear-to-cross-polarization transmission converter using ultrathin and smaller periodicity metasurface," *IEEE Antennas Wireless Propag. Lett.*, vol. 18, no. 7, pp. 1433–1437, 2019.
[26] Y. Li, Q. Cao, and Y. Wang, "A wideband multifunctional multilayer switchable linear polarization metasurface," *IEEE Antennas Wireless Propag. Lett.*, vol. 17, no. 7, pp. 1314–1318, 2018.
[27] S. Sun, W. Jiang, S. Gong, and T. Hong, "Reconfigurable linear-to-linear polarization conversion metasurface based on pin diodes," *IEEE Antennas Wireless Propag. Lett.*, vol. 17, no. 9, pp. 1722–1726, 2018.
[28] E. Arnieri, F. Greco, L. Boccia, and G. Amendola, "A SIW-Based polarization rotator with an application to linear-to-circular dual-band polarizers at $K-/Ka-$ band," *IEEE Trans. Antennas Propag.*, vol. 68, no. 5, pp. 3730–3738, 2020.
[29] M. Karamirad, C. Ghobadi, and J. Nourinia, "Metasurfaces for wideband and efficient polarization rotation," *IEEE Trans. Antennas Propag.*, vol. 69, no. 3, pp. 1799–1804, 2021.
[30] A. A. Omar, Z. Shen, and S. Y. Ho, "Multiband and wideband 90° polarization rotators," *IEEE Antennas Wireless Propag. Lett.*, vol. 17, no. 10, pp. 1822–1826, 2018.
[31] J. Wang, Z. Shen, and W. Wu, "Cavity-based high-efficiency and wideband 90° polarization rotator," *Appl. Phys. Lett.*, vol. 17, no. 10, pp. 1822–1826, 2018.
[32] T.-K. Wu, "Meander-line polarizer for arbitrary rotation of linear polarization," *IEEE Microw. Guided Wave Lett.*, vol. 4, no. 6, pp. 199–201, 1994.
[33] R. Bayderkhani, K. Forooraghi, and B. Abbasi-Arand, "Gain-enhanced SIW cavity-backed slot antenna with arbitrary levels of inclined polarization," *IEEE Antennas Wireless Propag. Lett.*, vol. 14, pp. 931–934, 2015.
[34] C.-A. Yu *et al.*, "24 GHz horizontally polarized automotive antenna arrays with wide fan beam and high gain," *IEEE Trans. Antennas Propag.*, vol. 67, no. 2, pp. 892–904, 2019.
[35] H. L. Zhu *et al.*, "Polarization-rotated waveguide antennas for base-station applications," *IEEE Antennas Wireless Propag. Lett.*, vol. 16, pp. 1545–1548, 2017.
[36] C. A. Balanis, *Antenna Theory: Analysis and Design,* 3rd. New York: Wiley, 2005.
[37] A. Ludwig, "The definition of cross polarization," *IEEE Trans. Antennas Propag.*, vol. 21, no. 1, pp. 116–119, 1973.
[38] A. T. Mobashsher, K. S. Bialkowski, and A. M. Abbosh, "Design of compact cross-fed three-dimensional slot-loaded antenna and its application in wideband head imaging system," *IEEE Antennas Wireless Propag. Lett.*, vol. 15, pp. 1856–1860, 2016.
[39] A. Mirbeik-Sabzevari, S. Li, E. Garay, H.-T. Nguyen, H. Wang, and N. Tavassolian, "Synthetic ultra-high-resolution millimeter-wave imaging for skin cancer detection," *IEEE Trans. Biomed. Eng.*, vol. 66, no. 1, pp. 61–71, 2019.

Shu-Lin Chen (M'20) was born in Hubei Province, China. He received the B.S. degree in electrical engineering from Fuzhou University (FZU), China, in 2012; the M.S. degree in electromagnetic field and microwave technology from Xiamen University (XMU), China, in 2015; and the Ph.D. degree in engineering from the University of Technology Sydney (UTS), Australia, in 2019.

From April to July 2019, he was a Research Associate with the State Key Laboratory of Terahertz and Millimeter Waves, City University of Hong Kong (CityU). Since September 2019, he has been a Postdoctoral Research Associate with the Global Big Data Technologies Centre (GBDTC), UTS, Australia. His research interests include reconfigurable antennas, leaky-wave antennas, and millimeter-wave antennas.

Dr Chen was a recipient of the Excellent Master's Thesis of Fujian Province in 2015. He was the corecipient for a number of international conference paper awards, including the Honorable Mention Award in *IEEE AP-S/URSI 2017*, the Best Paper Award Finalists in *ISAP 2017*, the Best Paper Award in *ISAPE 2018*, and the First Prize of Student Paper in *ACES-China 2021*. He was awarded the TICRA-EurAAP Travel Grant for the *EuCAP 2022*. He received the Outstanding Reviewer Awards in both 2019 and 2020 from the *IEEE Antennas and Wireless Propagation Letters*.

Geng-Bo Wu (S'19, M'21) received the B.Eng. and M.Sc. degrees from the University of Electronic Science and Technology of China, Chengdu, China, in 2015 and 2018, respectively, and the Ph.D. degree from the City University of Hong Kong (CityU), Hong Kong, in 2021.

In 2018, he was a Research Assistant with the State Key Laboratory of Terahertz and Millimeter Waves, CityU. He is now a Postdoctoral Research Fellow with the State Key Laboratory of Terahertz and Millimeter Waves, CityU. He has authored and co-authored for more than 40 peer-reviewed journal and conference papers. His research interests include millimeter-wave/THz antennas, metasurfaces, and imaging.

He was the recipient of the Finalist of the Best Student Paper Award in the 14$^{\text{th}}$ European Conference on Antennas and Propagation (EuCAP 2020), the Honorable Mention in the 2020 IEEE AP-S Internaitonal Symposium on Antennas and Propagation Student Paper Contest. He servers as a Reviewer for serveral journals and international conferences, including *IEEE TRANSATIONS ON ANTENNAS AND PROPAGATION, IEEE COMMUNICATIONS MAGAZINE, JOURNAL OF LIGHTWAVE TECHNOLOGY and EUCAP*.

Hang Wong received the B.Eng., M.Phil., and Ph.D. degrees in electronic engineering from City University of Hong Kong in 1999, 2002 and 2006, respectively. He joined the Department of Electrical Engineering at City University of Hong Kong in 2012. He had several visiting professorships at Stanford University, USA; University of Waterloo, Canada; University of College London, UK; and University of Limoges, France in the years of 2011, 2013, 2014, and 2015 respectively. Dr. Wong is the director of Applied Electromagnetics Laboratory at CityU; and the deputy director of the State Key Laboratory of Terahertz and Millimeter Waves (Hong Kong). His research interests are antenna technologies of 5G, 6G, millimeter-wave and terahertz applications. His achievements led to receiving numerous awards at local, national and international conferences. For example, he received the best paper award at the national conference 2017 *Les Journées Nationales Microondes* in France; the best paper award at the 2017 *IEEE International Workshop on Electromagnetics* in the UK; the best associate editor award 2016 of an *IEEE Antennas and Wireless Propagation Letters* in the US; and an outstanding scientist award of 2016 in Shenzhen city presented by Shenzhen Science and Technology Bureau. He was awarded to lead a major project supported by the Ministry of Industry and Information Technology of PRC to develop new antenna elements for TD-LTE and 5G applications. He has over 200 publications, 2 co-authors of book chapters and 20 US and China patents. He is the chair of the IEEE Hong Kong Section of the Antennas and Propagation (AP)/Microwave Theory and Techniques (MTT) Chapter. He is the IEEE APS Region-10 Representative. He is an associate editor of IEEE Transactions on Antennas and Propagation and was the associate editor of IEEE Antennas and Wireless Propagation Letters. Dr. Wong was the General Co-chair of the Asia Pacific Microwave Conference (AMPC) 2020, Hong Kong; and the General Chair of Cross-Strait Radio Science and Wireless Technology Conference 2021, Shenzhen, China.

Bao Jie Chen (M' 18) was born in Liaoning, China, in 1984. He received the B.S. and M.S. degrees in material science from Dalian Polytechnic University, Dalian, China, in 2007 and 2010, respectively, and the Ph.D. degree in electrical engineering from the City University of Hong Kong, Hong Kong, in 2014.

He is currently an Engineer with the State Key Laboratory of Terahertz and Millimeter Waves in City University of Hong Kong. His current research interests include rare-earth-doped materials, optical amplifiers, and development of terahertz devices and components.

Chi Hou Chan (S'86–M'86–SM'00–F'02) received the B.S. and M.S. degrees in electrical engineering from the Ohio State University, Columbus, OH, USA, in 1981 and 1982, respectively, and the Ph.D. degree in electrical engineering from the University of Illinois, Urbana, IL, USA, in 1987.

From 1987 to 1989, Dr. Chan was a Visiting Assistant Professor in the Department of Electrical and Computer Engineering at the University of Illinois. He joined the Department of Electrical Engineering at the University of Washington, Seattle, WA, USA in 1989 and was promoted to Associate Professor with tenure in 1993. In 1996, he joined the Department of Electronic Engineering, City University of Hong Kong (CityU) as Professor and was promoted to Chair Professor of Electronic Engineering in 1998. From 1998 to 2009, he was first Associate Dean and then Dean of College of Science and Engineering at CityU. He also served as Acting Provost of the university from July 2009 to September 2010. He is currently the Director of State Key Laboratory of Terahertz and Millimeter Waves (City University of Hong Kong). His current research interests include computational electromagnetics, millimeter-wave circuits and antennas, and terahertz science and technology.

Professor Chan was elected an IEEE Fellow in 2002, with the citation of "For Contributions to Computational Electromagnetics". He received the 2019 IEEE Antennas and Propagation Society Harrington-Mittra Computational Electromagnetics Award for his fundamental contributions to fast solutions of integral equations using FFT with applications to scattering, antennas and interconnect structures in homogeneous and layered medium. He is also bestowed with the 2019 Distinguished Alumni Award from the Department of Electrical and Computer Engineering, University of Illinois at Urbana-Champaign.

Y. Jay Guo (Fellow'2014) received a Bachelor's Degree and a Master's Degree from Xidian University in 1982 and 1984, respectively, and a Ph.D Degree from Xian Jiaotong University in 1987, all in China. His research interests include antennas, mm-wave and THz communications and sensing systems as well as big data technologies. He has published five books and over 600 research papers including over 280 IEEE Transactions papers, and he holds 26 international patents. He is a Fellow of the Australian Academy of Engineering and Technology, a Fellow of IEEE and a Fellow of IET, and was a member of the College of Experts of Australian Research Council (ARC, 2016-2018). He has won a number of the most prestigious Australian national awards including the Engineering Excellence Awards (2007, 2012) and CSIRO Chairman's Medal (2007, 2012). He was named one of the most influential engineers in Australia in 2014 and 2015, and one of the top researchers across all fields in Australia in 2020 and 2021, respectively. Together with his students and postdocs, he has won numerous best paper awards.

He is a Distinguished Professor and the Director of Global Big Data Technologies Centre (GBDTC) at the University of Technology Sydney (UTS), Australia. He is the founding Technical Director of the New South Wales Connectivity Innovation Network. Prior to joining UTS in 2014, he served as a Director in CSIRO for over nine years. Before joining CSIRO, he held various senior technology leadership positions in Fujitsu, Siemens and NEC in the U.K.

Prof Guo has chaired numerous international conferences and served as a guest editor for a number of IEEE publications. He was the Chair of International Steering Committee, International Symposium on Antennas and Propagation (2019-2021). He has been the International Advisory Committee Chair of IEEE VTC2017, General Chair of ISAP2022, ISAP2015, iWAT2014 and WPMC'2014, and TPC Chair of 2010 IEEE WCNC, and 2012 and 2007 IEEE ISCIT. He served as Guest Editor of special issues on "*Low-Cost Wide-Angle Beam Scanning Antennas*", "*Antennas for Satellite Communications*" and "*Antennas and Propagation Aspects of 60-90GHz Wireless Communications*," all in IEEE Transactions on Antennas and Propagation, Special Issue on "*Communications Challenges and Dynamics for Unmanned Autonomous Vehicles*," IEEE Journal on Selected Areas in Communications (JSAC), and Special Issue on "*5G for Mission Critical Machine Communications*", IEEE Network Magazine.